electronics

MDPI

Article

Diffmap: Enhancement Difference Map for Peripheral Prostate Zone Cancer Localization Based on Functional Data Analysis and Dynamic Contrast Enhancement MRI

Roman Surkant [1,*], **Jurgita Markevičiūtė** [2], **Ieva Naruševičiūtė** [3], **Mantas Trakymas** [3], **Povilas Treigys** [1] and **Jolita Bernatavičienė** [1]

[1] Institute of Data Science and Digital Technologies, Faculty of Mathematics and Informatics, Vilnius University, 08412 Vilnius, Lithuania; povilas.treigys@mif.vu.lt (P.T.); jolita.bernataviciene@mif.vu.lt (J.B.)
[2] Institute of Applied Mathematics, Faculty of Mathematics and Informatics, Vilnius University, 03225 Vilnius, Lithuania; jurgita.markeviciute@mif.vu.lt
[3] National Cancer Institute, 08406 Vilnius, Lithuania; ieva.naruseviciute@nvc.santa.lt (I.N.); mantas.trakymas@nvc.santa.lt (M.T.)
* Correspondence: roman.surkant@mif.stud.vu.lt

Abstract

Dynamic contrast-enhancement (DCE) modality of MRI is typically considered secondary in prostate cancer (PCa) diagnostics, due to the common interpretation that its diagnostic power is lower than that of other modalities like T2-weighted (T2W) or diffusion-weighted imaging (DWI). To challenge this paradigm, this study introduces a novel concept of a difference map, which relies exclusively on DCE-MRI for the localization of peripheral zone prostate cancer using functional data analysis-based (FDA) signal processing. The proposed workflow uses discrete voxel-level DCE time–signal curves that are transformed into a continuous functional form. First-order derivatives are then used to determine patient-specific time points of greatest enhancement change that adapt to the intrinsic characteristics of each patient, producing diffmaps that highlight regions with pronounced enhancement dynamics, indicative of malignancy. A subsequent normalization step accounts for inter-patient variability, enabling consistent interpretation across subjects and probabilistic PCa localization. The approach is validated on a curated dataset of 20 patients. Evaluation of eight workflow variants is performed using weighted log loss, the best variant achieving a mean log loss of 0.578. This study demonstrates the feasibility and effectiveness of a single-modality, automated, and interpretable approach for peripheral prostate cancer localization based solely on DCE-MRI.

Keywords: cancer localization; dynamic contrast enhancement; functional data analysis; image processing; image subtraction; MRI; peripheral zone; prostate cancer

Check for updates

Academic Editor: Yoichi Tomioka

Received: 9 December 2025
Revised: 20 January 2026
Accepted: 22 January 2026
Published: 24 January 2026

1. Introduction

Prostate cancer (PCa) is among the most frequently diagnosed malignancies globally [1]. It ranks fourth in cancer incidence across the whole population, with 1.5 million new cases reported in 2022. Among males, PCa is the second most commonly diagnosed cancer, affecting almost a third of the population. Although the mortality rates are relatively lower compared to other cancer types, it is still critical to ensure accurate and timely diagnosis of prostate cancer.

Currently, the diagnostic process is guided by the Prostate Imaging Reporting and Data System (PI-RADS), which provides a standardized framework for image acquisition and

https://doi.org/10.3390/electronics15030507

interpretation of prostate MRI [2,3]. It is based on multiparametric MRI (mpMRI), which incorporates several imaging sequences: T2-weighted (T2W), diffusion-weighted imaging (DWI), and dynamic contrast enhancement (DCE). T2W imaging provides high-resolution anatomic detail and depicts prostate cancer as areas of hypointensity due to increased cellularity and reduced water content, although its performance is limited in the transition zone. DWI assesses tissue cellularity by measuring water molecule motion, which is more restricted in cancer, making DWI particularly valuable in the transition zone and improving diagnostic specificity when combined with T2-weighted imaging. DCE imaging evaluates differences in contrast uptake kinetics between malignant and benign tissue, reflecting tumor angiogenesis, though overlap may occur with benign inflammatory processes such as prostatitis [4]. While all three sequences are used in clinical evaluation, only T2W and DWI are classified as primary modalities. DCE is regarded as secondary and is typically used for diagnostic validation or as a "back-up" when primary modalities are degraded [2]. Motivated by this clinical gap, we investigate whether DCE contains sufficient diagnostic signal for tumor localization when analyzed as voxel-wise enhancement dynamics, rather than as a supportive sequence.

Due to a limited role of DCE in diagnostics, several studies have explored biparametric MRI (bpMRI), which excludes the DCE modality based on bpMRI requiring reduced examination time, elimination of contrast agent administration, and comparable diagnostic performance relative to mpMRI [5]. Several literature reviews have examined comparative studies between mpMRI and bpMRI, generally concluding that the diagnostic accuracy is similar between the two approaches [6,7]. These conclusions have also been criticized for methodological heterogeneity and under-reporting of clinical details, casting doubt on the reliability of those findings [8].

An important part of the PI-RADS assessment is determining the lesion's location within the prostate—whether in the peripheral zone (PZ) or the transition zone (TZ)—as there are biological and epidemiological differences between these regions [9]. The majority of PCa cases originate in PZ rather than TZ [2,10]. Furthermore, lesions located in PZ are associated with poorer clinical outcomes and higher levels of malignancy compared to those in TZ [11]. It is also important to consider zone-specific benign abnormalities that may mimic malignancy, leading to false-positive findings—benign prostatic hyperplasia (BPH), commonly occurring in TZ, and prostatitis, mostly affecting PZ [2].

This study demonstrates an application of functional data analysis (FDA), a subfield of statistics for analysis of data in the form of functions (or curves) [12]. FDA has been applied in a broad range of domains [13], including biomedical science. For instance, forecasting of breast cancer mortality rates [14], analysis of corneal curvature maps [15], modeling of heart rate dynamics [16], denoising of functional MRI (fMRI) signals through smoothing [17], and functional embedding in genomics [18]. To the best knowledge of the authors, there are no known studies involving FDA methods applied in the domain of prostate cancer.

According to PI-RADS, dynamic contrast curves can be categorized into three types as follows: type 1 (progressive), characterized by a continuous increase in enhancement level over time; type 2 (plateau), when enhancement level stabilizes after an initial rise; and type 3 (wash-in and wash-out), characterized by a decline in enhancement level after an initial rise [2,19]. The DCE curve characteristics assist in differentiating PCa from benign tissue—type 3 curves are typically associated with malignancy. Due to the heterogeneous nature of enhancement patterns in PCa, there is no strong evidence supporting curve type analysis for definitive diagnosis.

Prostate cancer exhibits pronounced biological and imaging heterogeneity, which substantially complicates diagnostic accuracy. Systematic biopsy remains an important complement to targeted approaches, as it can partially mitigate sampling bias caused by spatial and multifocal tumor heterogeneity [20]. Among mpMRI features, apparent diffusion coefficient (ADC) heterogeneity shows the strongest clinical relevance, particularly in the TZ, whereas heterogeneity on T2W and DCE imaging appears to reflect generalized tissue complexity rather than directly affecting cancer detection. At the molecular level, PCa demonstrates significant clinical, spatial, and morphological heterogeneity, leading to biopsy undersampling, grading variability, and discordance between histopathology and the true genomic landscape of the tumor [21]. Zonal differences further complicate diagnostics: approximately 80% of PCa appears in the PZ and 15% in the TZ, yet TZ cancers contribute disproportionately to mortality due to confounding benign prostatic hyperplasia [22]. Age-related tissue characteristics and prostatitis may additionally mimic malignant imaging features, increasing the risk of PI-RADS misclassification [23]. Interpretation of mpMRI is further limited by inter-reader variability, with reported PI-RADS agreement ranging from 33% to 86% and only moderate overall concordance with a kappa of 0.53 [24]. Moreover, PI-RADS three lesions account for approximately 17% of examinations, while only 15–20% represent clinically significant PCa, highlighting persistent diagnostic uncertainty in equivocal cases [25].

Current literature on prostate cancer diagnosis is predominantly aimed at lesion classification, which generally requires manually outlined regions of interest (ROI) [26–32]. In contrast, our study eliminates this dependency and is aimed at doing lesion localization, thereby identifying ROIs without manual intervention. Some works have investigated localization, such as [33], where pharmacokinetic parameters are derived from the DCE modality for tumor identification, and [34], where prostate gland segmentation is done from ROI-based radiomic features derived from DCE subtraction maps. In contrast, our method operates directly on the raw DCE time–signal data and dynamically adapts subtraction time moments to each patient. In addition, our approach challenges the prevailing assumption that effective diagnostic performance requires data from multiple MRI sequences or that dynamic contrast imaging lacks diagnostic power. The purpose of our research is to maximize the diagnostic utility of exclusively DCE MRI. Finally, a methodological novelty is also introduced by using functional data analysis for the processing of DCE time–signal curves in a manner that automatically adapts to patient-specific enhancement patterns.

This study presents a workflow for analyzing DCE MRI of the prostate's peripheral zone, without reliance on other mpMRI modalities such as T2W or DWI. Time–signal intensity curves are generated voxel-wise across all slices and transformed into continuous functional form, from which first-order derivatives are calculated. These derivatives are aggregated per slice, and the resulting curves are combined to identify optimal time points for image subtraction. Subtraction produces difference maps (or diffmaps) that quantify the magnitude of enhancement change. Following inter-slice normalization, the normalized diffmaps highlight regions with enhancement patterns indicative of malignancy.

2. Materials and Methods

The proposed method uses three inputs: MRI-DCE imaging sequence, peripheral zone (PZ) masks, and cancer masks. The latter is used as the ground truth for performance evaluation. PZ masks are used for spatial filtering and are obtained using a combination of expert manual annotations by two radiologists with 10 and 15 years of experience, and automated neural network-based segmentation [35]. All automatically generated masks were subsequently validated by radiologists to ensure clinically reliable delineations. An overlay of a sample of data of a single DCE slice with PZ and PCa contours is shown in Figure 1. The dataset within the scope of our research was provided by the Lithuanian National Cancer Institute (NVI) under the terms of the bioethical agreement 2020/5-1229-714. It comprises a total of 144 patients from 11 distinct clinical centers and includes scans acquired on MRI systems from three different vendors. The clinical study was conducted at NVI, where MRI-guided targeted biopsies were performed for all patients. However, the proposed methodology requires the availability of PZ masks. Consequently, only a subset of 20 patients met all the necessary criteria for further analysis.

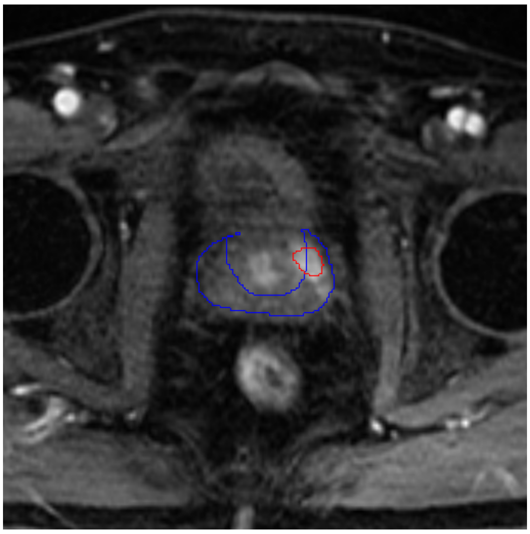

Figure 1. Overlay of a DCE image of a select patient, slice, and time moment with contours for peripheral zone (blue) and cancer lesion (red) masks.

This research proposes a workflow for processing DCE data of a patient to generate regions of suspicion for malignancy. The diagram of the workflow is shown in Figure 2, which consists of 11 transformational steps and one additional step for evaluation. Transformational steps can be grouped into three stages: time point calculation, image subtraction, and distribution normalization. More detailed descriptions for each step are provided in the following sections.

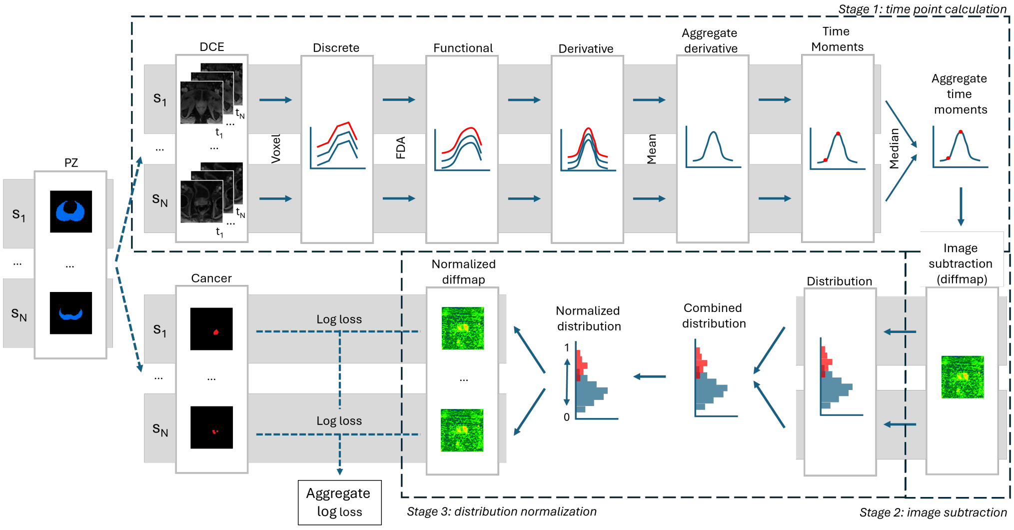

Figure 2. Workflow diagram. Three stages consisting of 11 steps to process and evaluate a single patient.

While the workflow requires a PZ mask as input, all subsequent processing steps are fully automated and do not require manual lesion delineation or user interaction.

Notation use in the article: patient identifier p, representing a specific patient in the dataset; slice index s, referring to a particular slice in patient's MRI volume; time index t, referring to the discrete time moment of DCE image acquisition; MRI-DCE imaging

$E(p,s,t)$, a mpMRI modality representing contrast enhancement over time consisting of a set of grayscale images for patient p, slice s, and time moment t; PZ mask $Z(p,s)$, a binary mask indicating the peripheral zone region; cancer mask $C(p,s)$, a binary mask indicating the ground truth PCa region.

2.1. Time Point Calculation

The main purpose of this stage is to use voxel intensity in the peripheral zone of DCE imaging of a patient to determine specific time points that indicate a temporal interval with the most significant change in enhancement level.

Voxel-level time series. Given a patient p, only the peripheral zone is considered from each DCE slice: $E(p,s,t) \cap Z(p,s)$. Discrete time series of DCE intensities (or time–signal curves) are then constructed at a voxel level. Each curve represents the enhancement level at a specific coordinate of the slice s at different time indices t. An example output is shown in Figure 3a, where a random sample of 10 curves shows the DCE signal value at 31 time moments.

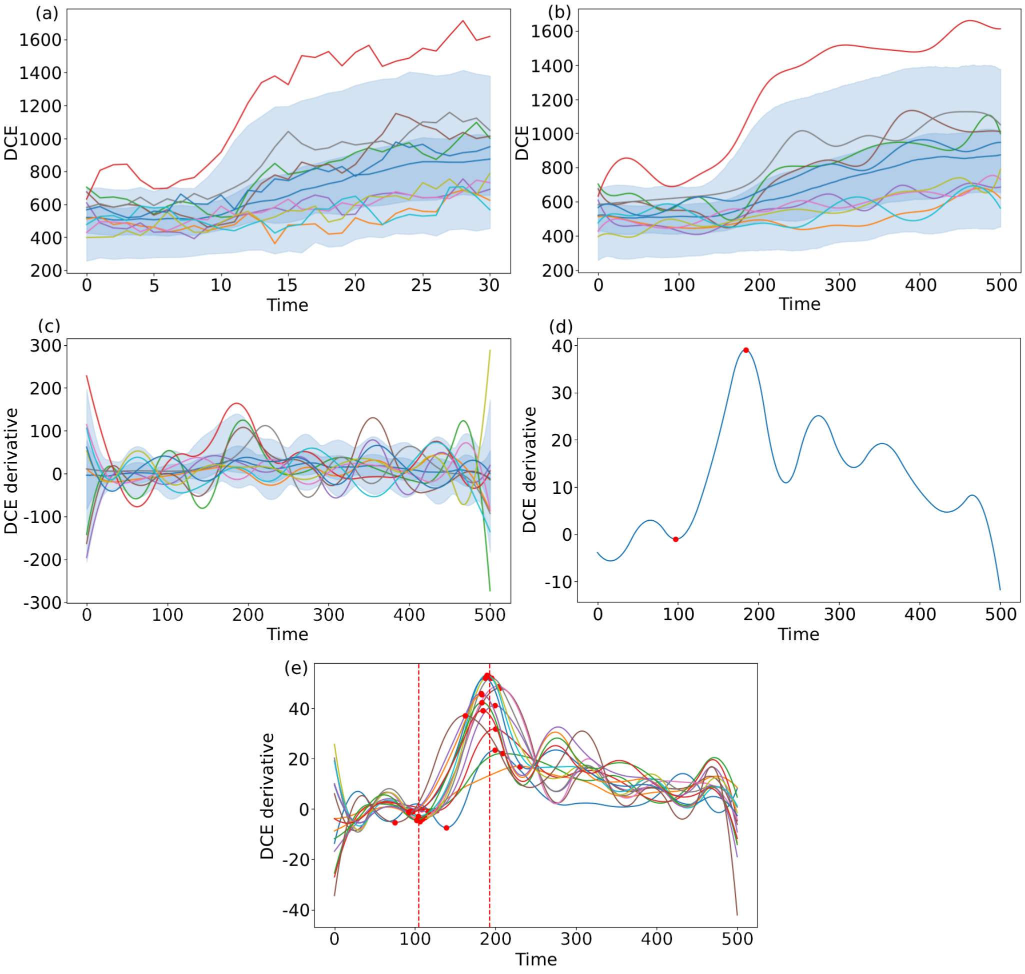

Figure 3. Example output from each step of the first stage (time point calculation) of the workflow. (**a**) Example of a random sample of 10 curves (original, discrete DCE time–signal) from patient 028, slice 23. (**b**) Functional form of the curve sample in (**a**). (**c**) Functional derivative of the curve sample in (**b**). Blue and light blue shaded areas indicate the 25th–75th and 5th–95th percentile ranges, respectively. (**d**) Average derivative curve for the slice. Red points represent slice-level time points $t_0(p,s)$ and $t_1(p,s)$. (**e**) Average derivative curves for all slices. Red dashed lines represent median, patient-level time points $t_0(p)$ and $t_1(p)$.

Functional representation. The discrete curves are transformed into a functional form—a continuous curve representing interpolated movement of dynamic contrast. Functional forms are constructed with 14 B-spline basis functions of order 4 using the *scikit-fda* package (version 0.10.1). An example is shown in Figure 3b, where the same sample of 10 curves is represented as continuous functions (approximated by 501 time moments). The parameters of functional smoothing were determined using the Root Mean Square Error (RMSE) as a quantitative measure of the deviation between the functional curve and the original discrete curve. To ensure dimensional consistency, the original curve was upsampled via linear interpolation. Figure 4 shows an RMSE contour map, indicating which combinations of parameters have the lowest deviation. The green dot represents the minimum point of RMSE and our spline parameter choice.

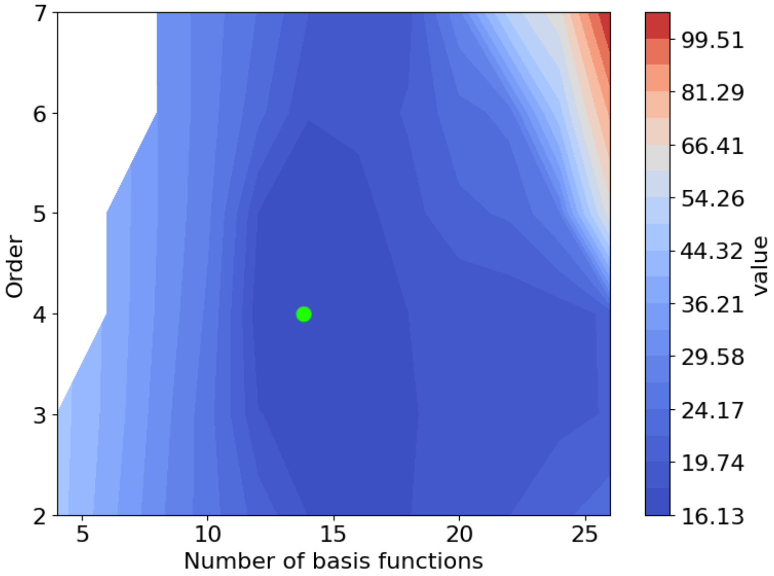

Figure 4. Contour plot of the parameter space used for functional transformation, where contours represent global average deviation between the original DCE signal curve and its functional representation measured in Root Mean Square Error (RMSE). The green dot represents the minimum RMSE point of 14 basis functions of order 4.

Functional derivative. Each functional curve is further converted into its first-order derivative to capture the rate of change in signal intensity over time. An example output is shown in Figure 3c, where each curve of the corresponding color from the previous graph represents the rate of signal change of the continuous function.

Time point selection. Two specific time points $t_0(p), t_1(p)$ are chosen for the purpose of DCE slice subtraction in the next stage of the workflow. These time points are chosen to correspond to the period of greatest contrast change, enabling identification of regions exhibiting the most pronounced dynamic behavior.

The process for time point selection is as follows: (1) derivative curves are averaged across all voxels within each slice, yielding a single average derivative curve per slice (example shown in Figure 3d) ; (2) initial slice-level time points $t_0(p,s), t_1(p,s)$ are identified based on the set of average derivative curves; and (3) patient-level time points $t_0(p), t_1(p)$ are determined by taking the median across all slice-level time points (see example in Figure 3e) for each respective time point, as shown in the following Equation (1):

$$t_0(p) = \operatorname{med}\Big(\bigcup_s t_0(p,s)\Big) \qquad t_1(p) = \operatorname{med}\Big(\bigcup_s t_1(p,s)\Big) \tag{1}$$

Two variants for determining time moments $t_0(p,s), t_1(p,s)$ are considered as follows:

- "peak-drop": the time point corresponding to the maximum value of the derivative curve is selected as $t_1(p,s)$ and the first preceding local minimum ("valley") is selected as $t_0(p,s)$;
- "peak-start": the time points corresponding to the maximum derivative value are selected as $t_1(p,s)$ and the earliest available DCE time moment is selected as $t_0(p,s)$.

A visual comparison of the two variants is demonstrated in Figure 5.

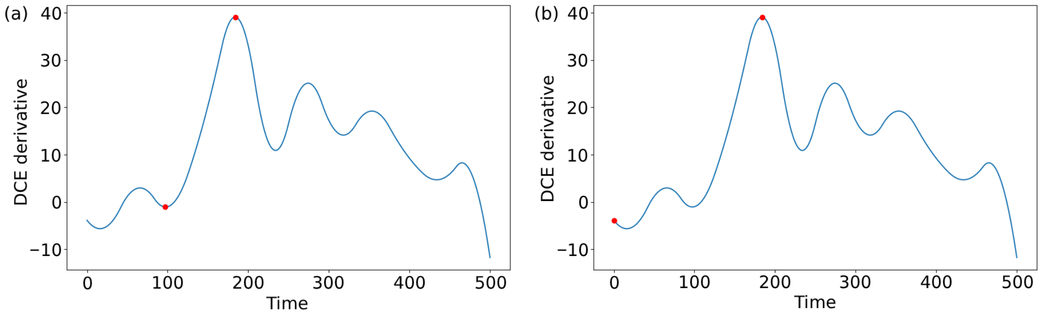

Figure 5. Examples of slice-level time point selection variants for a selected slice and patient. Red points indicate $t_1(p,s)$ (rightmost) and $t_0(p,s)$ (leftmost). (**a**) Peak-drop variant. (**b**) Peak-start variant.

Due to potential instability at the boundaries of functional derivatives, the first and last 10% of each curve are excluded from consideration of time point selection (except for $t_0(p,s)$ in the "peak-start" variant).

Such a time point selection algorithm is fully automated and adapts to the enhancement dynamics specific to each patient, irrespective of the time scale or magnitude of the enhancement signal. It requires no manual intervention or parameter tuning.

2.2. Image Subtraction

Image subtraction is a technique in which the pixel intensity values of one image are subtracted from the corresponding pixels of another image. This method has been employed in various domains, including medical imaging [26,36], to accentuate changes between images.

This technique is used to generate a difference map $D(p,s)$, or diffmap, which highlights the magnitude of change in enhancement levels between the two DCE slices on a voxel level. Image subtraction is performed on each slice of the patient between time points $t_0(p)$ and $t_1(p)$ as follows:

$$D(p,s) = E(p,s,t_1(p)) - E(p,s,t_0(p)).$$

The diffmap $D(p,s)$ may contain both positive and negative values, as the DCE signal of some voxels may have a decreasing trend. Two variants are considered for handling negative values as follows:

- "clipping": all negative values in $D(p,s)$ are substituted with a zero as follows:

$$D'(p,s) = \max(0, D(p,s))$$

- "non-clipping": all values remain as-is as follows:

$$D'(p,s) = D(p,s).$$

2.3. Distribution Normalization

It is hypothesized that malignancies are associated with more pronounced fluctuations in contrast enhancement. Since the diffmap $D(p,s)$ captures the most significant changes in enhancement levels, higher values in the diffmap are assumed to correlate with a higher likelihood of cancerous tissue.

By constructing a combined statistical distribution of $D'(p,s)$ voxel values within the peripheral zone (PZ) across an entire patient volume, it can be observed that higher values—those located near the upper tail of the distribution—are more likely to represent PCa, whereas lower values—closer to the lower tail—are more indicative of healthy tissue. An illustrative example of such distributions is provided in Figure 6.

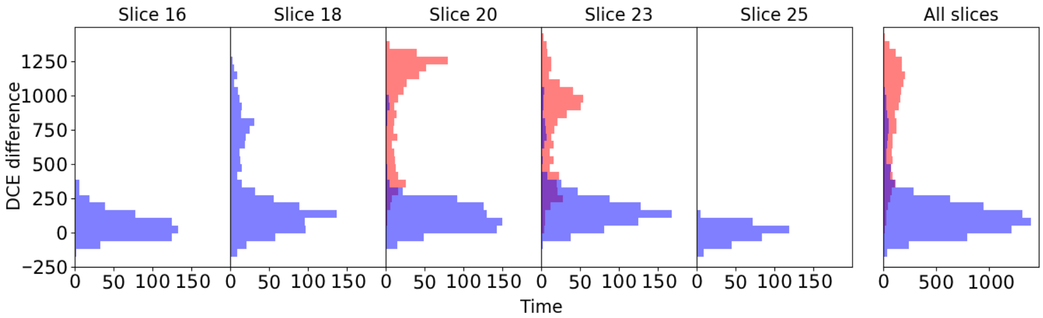

Figure 6. Histogram of voxel value distributions from selected slices of a patient and a histogram for the entire patient volume. Malignant voxels (red), benign voxels (blue).

To facilitate the comparison of diffmap values across patients—particularly given inter-patient variability in dynamic contrast-enhanced signal scales—distribution normalization is applied at the patient level to generate a normalized distribution $D''(p)$. This normalization harmonizes the dynamic range of enhancement variations and allows for consistent interpretation across subjects. Two normalization variants are considered:

- Min-max normalization: the distribution is rescaled to a range $[0,1]$. Intermediate values are linearly adjusted as follows:

$$D''(p,s) = \frac{D'(p,s) - \min(\bigcup_s D'(p))}{\max(\bigcup_s D'(p) - \min(\bigcup_s D'(p))}$$

- Percentile ranking: all values are ranked based on their value within the distribution. Ranks are then normalized by dividing by the total number of values as follows:

$$D''(p,s) = \frac{\text{rank}_p(D'(p,s)) - 1}{N-1}.$$

The min-max approach preserves relative spacing between values of the distribution, but it is sensitive to outliers, which may distort the distribution. The percentile ranking approach is robust to outliers, as it relies on the relative positioning of the values in the distribution, rather than absolute magnitude.

2.4. Evaluation

To quantitatively estimate the performance of our proposed approach and select the best workflow variants, logarithmic loss (or log loss) is used as the primary evaluation metric. It is often used in machine learning to quantify the divergence between predicted probabilities and actual binary labels. In this study, ground truth is a binary outcome of overlap with the cancer mask $C(p,s)$, while the predicted probabilities correspond to the normalized distribution values of $D''(p)$. This metric is particularly suitable in our context, as the objective is to evaluate the degree of separation between benign and malignant regions and ensure that the model concentrates voxels overlapping with $C(p,s)$ closer to the top tail of the distribution and voxels not overlapping with $C(p,s)$—near the bottom tail of the distribution. Strongly incorrect predictions (e.g., assigning a very low probability to a PCa voxel) are more heavily penalized.

The standard log loss is defined in Equation (2), where N is the number of samples (i.e., voxels), $y_i \in \{0,1\}$—true label, and $\hat{y}_i \in [0,1]$ is the predicted probability of positive class (i.e., malignancy).

$$\mathrm{L} = -\frac{1}{N}\sum_{i=1}^{N}[y_i \log(\hat{y}_i) + (1-y_i)\log(1-\hat{y}_i)] \tag{2}$$

$$\mathrm{wL} = -\frac{1}{N}\sum_{i=1}^{N} w_i[y_i \log(\hat{y}_i) + (1-y_i)\log(1-\hat{y}_i)] \tag{3}$$

Voxels overlapping with the PCa mask constitute only a small minority. Due to the substantial class imbalance, a weighted version of the log loss is used to ensure that misclassifying malignancy has a larger penalty despite significant under-representation in the dataset, and both classes contribute equally to the evaluation. The weighted log loss is defined in Equation (3), where w_i is the weight assigned to the i-th sample. These weights are inversely proportional to the frequency of each class within a patient's volume. For instance, if PCa voxels comprise 5% of all voxels for a patient, then each PCa prediction is weighted 20 times more than a non-cancerous voxel. Summary statistics on class imbalance and the corresponding weight ratios are presented in Table 1.

Table 1. Summary statistics of the number of voxels overlapping and not overlapping with the cancer mask.

	Min	**Mean**	**Max**
Cancer voxels	80	1987	10,131
Non-cancer voxels	7507	45,995	145,360
Cancer voxel ratio, %	0.2	4.7	26.3

3. Results

The proposed workflow comprises three modular components, each with two possible variants, resulting in a total of eight experimental configurations, which are shown in Table 2.

Log loss values are computed for each individual patient. To summarize overall accuracy over the whole dataset, the mean log loss and standard deviation of log loss are calculated, reflecting average performance and variability of performance estimates, respectively.

The resulting log loss values associated with each experimental configuration are presented in Table 2. The peak-start time point selection variant produces both a lower log loss mean and a lower log loss variance compared to analogous workflows of the peak-drop variants, likely due to a bigger enhancement level difference and a more significant wash-in change. The optimal set of variants consists of peak-start for time point selection, image subtraction without clipping, and min-max distribution normalization.

Table 2. Summary of performance evaluation for all 8 workflow experiment iterations. Best-performing results (lowest log loss mean and standard deviation) are marked in bold.

Time Point Selection Variant	Image Subtraction Variant	Distribution Normalization Variant	Log Loss μ	Log Loss σ
Peak-drop	Clipping	Min-max norm.	3.504	5.136
		Percentile rank.	0.713	0.240
	Non-clipping	Min-max norm.	0.609	0.143
		Percentile rank.	0.767	0.353
Peak-start	Clipping	Min-max norm.	1.600	2.697
		Percentile rank.	0.641	0.165
	Non-clipping	Min-max norm.	**0.578**	**0.112**
		Percentile rank.	0.647	0.180

Given the optimal workflow configuration, log loss values are calculated for each patient in the dataset to assess predictive performance at the individual level. For each patient, workflow predictions are compared with the corresponding ground truth by computing a voxel-wise weighted log loss over the entire patient volume, including all slices. The resulting patient-level loss is obtained by averaging the voxel-wise log loss values across the full volume. The resulting distribution is presented in Figure 7. Such a relative comparison of performance among patients is used for the qualitative analysis below.

Patient 026 shows the lowest log loss, indicating the highest prediction accuracy using the proposed approach. In contrast, patients 108 and 107 show the highest log losses, corresponding to the poorest performance among the patients.

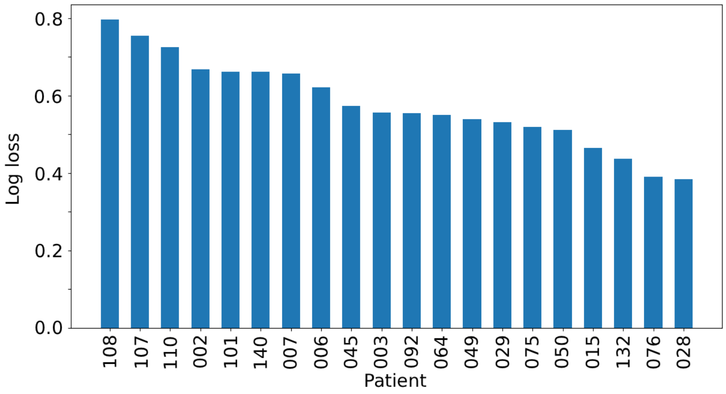

Figure 7. Log loss distribution among patients.

In addition, decision threshold-based metrics, Dice score, sensitivity, and specificity are calculated to assess localization accuracy and illustrate the trade-off between false positive and false negative voxel classification given a particular decision boundary. The results are shown in Figure 8. The highest Dice score is achieved with a threshold of 0.6, while the highest combined sensitivity and specificity is achieved with a threshold of 0.5. It should be noted that the Dice score measures only strict spatial overlap with the ground truth and does not account for proximity/near-miss predictions, which may still be clinically informative for radiologists; as a result, the metric can be overly penalizing in this context.

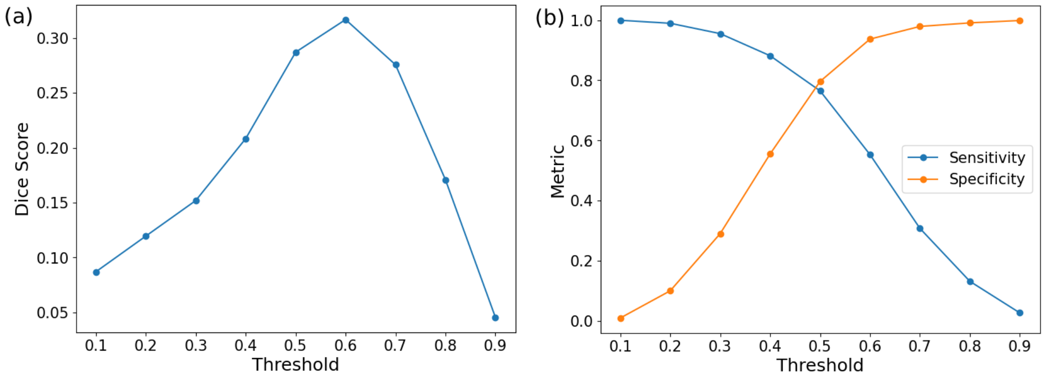

Figure 8. Additional quantitative metrics dependent on the decision threshold. (**a**) Dice score, (**b**) sensitivity and specificity.

Furthermore, a qualitative evaluation was also conducted. Figure 9 displays diffmaps for selected slices from two patients—one of high predictive power, and one of low. In these diffmaps, yellow and orange regions correspond to the upper tail of the distribution $D(p)$ (indicating high suspicion for malignancy), whereas green regions indicate areas closer to the lower tail of the distribution (low suspicion).

In the first case (Figure 9a), the lesion is located at the border of the peripheral and transition zones on the right side. The predicted high-suspicion region from our proposed model is entirely contained within the ground truth cancer mask, as indicated by dark yellow and orange regions. In the second case (Figure 9b), multiple lesions are present, one located entirely within the peripheral zone, and another primarily in the transition zone with minor extension into the peripheral zone. The model's predicted high-suspicion regions partially overlap with the PCa mask in the top two slices, while the overlap is minimal in the bottom two slices.

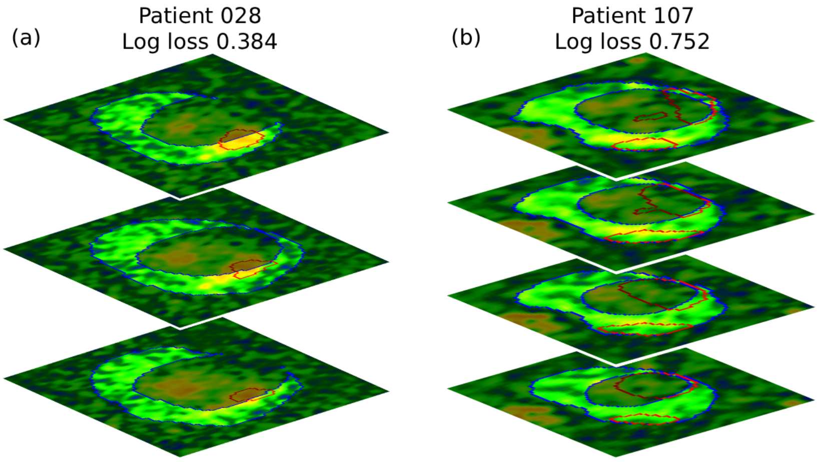

Figure 9. Qualitative evaluation of two patient cases—one with the lowest log loss value, and another with one of the highest—on select slices. Overlays indicate cancer (red) and peripheral zone (blue) contours. Heatmap colors range from green (low $D(p)$) to orange (highest values). (**a**) Patient 028, high accuracy case with log loss of 0.384. (**b**) Patient 107, low accuracy case with a log loss of 0.752.

These qualitative observations are consistent with the corresponding patient-level log loss values (0.384 for patient 028 vs. 0.752 for patient 107), where tighter spatial alignment between high-suspicion regions and ground truth masks results in lower penalization by the weighted log loss metric.

4. Discussion and Conclusions

This study introduces a diffmap, a novel method for localizing suspicious regions in the peripheral zone for prostate cancer lesion detection using only dynamic contrast-enhanced MRI data in conjunction with functional data analysis (FDA). Unlike traditional approaches that rely on multiparametric MRI, particularly T2-weighted and diffusion-weighted sequences, this method uses DCE data exclusively and eliminates the requirement for manually annotated ROIs. The approach demonstrates that meaningful lesion localization can be achieved through analysis of enhancement dynamics alone.

Diffmaps are generated through functional transformation of voxel time–signal curves, derivative-based time point selection, image subtraction, and distribution normalization. They highlight high-suspicion areas that align closely with annotated cancer masks and act as an instrument for localizing zones potentially associated with PCa.

Unlike most prostate MRI studies that rely on manually delineated ROIs [26–32] and models requiring multiparametric MRI inputs [5–7], the proposed approach performs voxel-wise localization without manual lesion annotation and uses DCE-MRI as the sole imaging modality. This contrasts with pharmacokinetic modeling approaches [33], which require physiological assumptions, whereas the present method leverages FDA to adaptively identify patient-specific enhancement dynamics.

Several methodological variants were explored. The optimal workflow variant (peak-start time point selection, non-clipped subtraction, and min-max normalization) achieved the lowest log loss values, both in terms of mean and standard deviation, which reflects consistent predictive accuracy across the patient cohort. Qualitative evaluation revealed that high-suspicion regions overlap with cancer masks and exhibit spatial coherence between adjacent slices. Even in cases of partial overlap with ground truth, highlighted regions were typically located in proximity to cancer masks, which suggests that the method is sensitive to tumor-adjacent tissue with atypical enhancement patterns.

The effectiveness of the proposed approach supports the hypothesis that temporal dynamics of contrast enhancement (rather than absolute signal intensity) carry meaningful information about microvascular behavior in peripheral zone prostate cancer. By focusing on derivative-based enhancement changes, the method captures early response patterns of the contrast enhancement.

Despite promising results, there are certain limitations. The inherent nature of a normalized distribution ensures that every diffmap contains both low- and high-suspicion regions, regardless of the actual presence of malignancy. This may lead to false positive detections in patients with no PCa lesions. Another limitation is that each voxel is analyzed independently, losing potentially valuable spatial context, which may increase thte workflow's robustness to imaging noise and inter-slice misalignment. The third limitation is the modest size of the dataset. Expanding the cohort, especially with cases from multiple institutions, would improve generalizability and reduce dataset-specific bias.

In addition, a set of potential improvement points is proposed for future development of this methodology as follows:

- Spatial context. The current approach treats individual voxels independently, without explicitly modeling spatial relationships between neighboring voxels or adjacent slices. Since adjacent voxels are often spatially and functionally connected, incorporating spatial context, such as neighborhood-based features or slice-wise dependencies, may improve robustness to noise and enhance the accuracy of PCa localization.
- Pharmacokinetic analysis. Other types of information can be derived from MRI-DCE, which may provide additional diagnostic value. For instance, pharmacokinetic parametric maps: K^{trans} (volume transfer between blood plasma and extracellular-extravascular space), k_{ep} (transfer rate between extracellular-extravascular space and

blood plasma), v_e (volume fraction of extracellular-extravascular space), v_p (volume fraction of plasma in the tissue).

- Other MRI data. The present model utilizes a single input of the dynamic contrast-enhanced MRI sequence. Augmenting the model with additional MRI modalities, such as T2-weighted or diffusion-weighted imaging (DWI), may increase the diagnostic power.
- Image registration. Patient motion during MRI acquisition can lead to misalignment and distortion between image data, particularly in DCE-MRI. As the proposed method relies on voxel-level precision, such discrepancies may reduce its predictive performance. Implementing image registration techniques to spatially align the images across time points could mitigate this issue.
- Sample size. Although the full dataset included 144 patients, expert-validated peripheral zone annotations were available for only 20 cases at the time of analysis. This study, therefore, represents a methodological validation on a curated subset, which limits statistical power and generalizability.

This work is not intended to replace mpMRI-based localization strategies, but to investigate whether DCE-MRI contains sufficient information for meaningful lesion localization under the aforementioned constraints. Direct comparison with existing mpMRI-based or ROI-driven methods is not straightforward due to differences in available diagnostic information. Future work will focus on evaluating the proposed approach in conjunction with, or alongside, mpMRI methods.

In summary, the results suggest that an FDA-based workflow for processing DCE-MRI is capable of accurately localizing PCa lesions within the peripheral zone, even in isolation from other MRI sequences. The findings support the potential of DCE-centric functional curve-based diagnostic tools for prostate imaging. Extended validation and methodological improvements may unlock clinical adoption of the proposed approach.

Author Contributions: Conceptualization, J.B. and P.T. methodology, R.S. and J.B.; software, R.S.; validation, J.M., I.N., and J.B.; formal analysis, R.S.; investigation, R.S.; resources, J.M. and P.T. data curation, I.N. and M.T.; writing—original draft preparation, R.S. and J.B.; writing—review and editing, J.M. and I.N.; visualization, R.S.; supervision, P.T. and J.B.; project administration, J.B. and M.T.; funding acquisition, P.T. All authors have read and agreed to the published version of the manuscript.

Funding: Research is funded by the Research Council of Lithuania under the Programme “University Excellence Initiatives” of the Ministry of Education, Science and Sports of the Republic of Lithuania (Measure No. 12-001-01-01-01 “Improving the Research and Study Environment”). Project No.: S-A-UEI-23-11.

Data Availability Statement: The datasets presented in this article are not readily available due to confidentiality restrictions arising from biomedical data-sharing agreements and patient privacy considerations. Requests to access the datasets should be directed to the corresponding author.

Conflicts of Interest: The authors declare no conflicts of interest.

References

1. Bray, F.; Laversanne, M.; Sung, H.; Ferlay, J.; Siegel, R.L.; Soerjomataram, I.; Jemal, A. Global cancer statistics 2022: GLOBOCAN estimates of incidence and mortality worldwide for 36 cancers in 185 countries. *CA Cancer J. Clin.* **2024**, *74*, 229–263.
2. Weinreb, J.C.; Barentsz, J.O.; Choyke, P.L.; Cornud, F.; Haider, M.A.; Macura, K.J.; Margolis, D.; Schnall, M.D.; Shtern, F.; Tempany, C.M.; et al. PI-RADS prostate imaging—Reporting and data system: 2015, version 2. *Eur. Urol.* **2016**, *69*, 16–40.
3. Turkbey, B.; Rosenkrantz, A.B.; Haider, M.A.; Padhani, A.R.; Villeirs, G.; Macura, K.J.; Tempany, C.M.; Choyke, P.L.; Cornud, F.; Margolis, D.J.; et al. Prostate imaging reporting and data system version 2.1: 2019 update of prostate imaging reporting and data system version 2. *Eur. Urol.* **2019**, *76*, 340–351. [CrossRef] [PubMed]

4. Launer, B.M.; Ellis, T.A.; Scarpato, K.R. A contemporary review: mpMRI in prostate cancer screening and diagnosis. *Urol. Oncol. Semin. Orig. Investig.* **2025**, *43*, 15–22.
5. Kuhl, C.K.; Bruhn, R.; Krämer, N.; Nebelung, S.; Heidenreich, A.; Schrading, S. Abbreviated biparametric prostate MR imaging in men with elevated prostate-specific antigen. *Radiology* **2017**, *285*, 493–505. [CrossRef]
6. Woo, S.; Suh, C.H.; Kim, S.Y.; Cho, J.Y.; Kim, S.H.; Moon, M.H. Head-to-head comparison between biparametric and multiparametric MRI for the diagnosis of prostate cancer: A systematic review and meta-analysis. *Am. J. Roentgenol.* **2018**, *211*, W226–W241.
7. Belue, M.J.; Yilmaz, E.C.; Daryanani, A.; Turkbey, B. Current status of biparametric MRI in prostate cancer diagnosis: Literature analysis. *Life* **2022**, *12*, 804. [CrossRef]
8. Greenberg, J.W.; Koller, C.R.; Casado, C.; Triche, B.L.; Krane, L.S. A narrative review of biparametric MRI (bpMRI) implementation on screening, detection, and the overall accuracy for prostate cancer. *Ther. Adv. Urol.* **2022**, *14*, 17562872221096377. [CrossRef]
9. Yu, X.; Liu, R.; Song, L.; Gao, W.; Wang, X.; Zhang, Y. Differences in the pathogenetic characteristics of prostate cancer in the transitional and peripheral zones and the possible molecular biological mechanisms. *Front. Oncol.* **2023**, *13*, 1165732. [CrossRef]
10. McNeal, J.E.; Redwine, E.A.; Freiha, F.S.; Stamey, T.A. Zonal distribution of prostatic adenocarcinoma: Correlation with histologic pattern and direction of spread. *Am. J. Surg. Pathol.* **1988**, *12*, 897–906. [CrossRef]
11. Sato, S.; Kimura, T.; Onuma, H.; Egawa, S.; Takahashi, H. Transition zone prostate cancer is associated with better clinical outcomes than peripheral zone cancer. *BJUI Compass* **2021**, *2*, 169–177. [CrossRef]
12. Wang, J.-L.; Chiou, J.-M.; Müller, H.-G. Functional data analysis. *Annu. Rev. Stat. Appl.* **2016**, *3*, 257–295. [CrossRef]
13. Ullah, S.; Finch, C.F. Applications of functional data analysis: A systematic review. *BMC Med. Res. Methodol.* **2013**, *13*, 43. [CrossRef]
14. Erbas, B.; Akram, M.; Gertig, D.M.; English, D.; Hopper, J.L.; Kavanagh, A.M.; Hyndman, R. Using functional data analysis models to estimate future time trends in age-specific breast cancer mortality for the United States and England—Wales. *J. Epidemiol.* **2010**, *20*, 159–165. [CrossRef]
15. Locantore, N.; Marron, J.S.; Simpson, D.G.; Tripoli, N.; Zhang, J.T.; Cohen, K.L.; Boente, G.; Fraiman, R.; Brumback, B.; Croux, C.; et al. Robust principal component analysis for functional data. *Test* **1999**, *8*, 1–73. [CrossRef]
16. Ratcliffe, S.J.; Leader, L.R.; Heller, G.Z. Functional data analysis with application to periodically stimulated foetal heart rate data. I: Functional regression. *Stat. Med.* **2002**, *21*, 1103–1114. [CrossRef] [PubMed]
17. Vakorin, V.A.; Borowsky, R.; Sarty, G.E. Characterizing the functional MRI response using Tikhonov regularization. *Stat. Med.* **2007**, *26*, 3830–3844. [CrossRef] [PubMed]
18. Wu, P.-S.; Müller, H.-G. Functional embedding for the classification of gene expression profiles. *Bioinformatics* **2010**, *26*, 509–517. [CrossRef] [PubMed]
19. Hansford, B.G.; Peng, Y.; Jiang, Y.; Vannier, M.W.; Antic, T.; Thomas, S.; McCann, S.; Oto, A. Dynamic contrast-enhanced MR imaging curve-type analysis: Is it helpful in the differentiation of prostate cancer from healthy peripheral zone? *Radiology* **2015**, *275*, 448–457. [CrossRef]
20. Chen, C.; Yang, Z.; Sweeney, E.; Hectors, S.J.; Hu, J.C.; Margolis, D.J. Prostate heterogeneity correlates with clinical features on multiparametric MRI. *Abdom. Radiol.* **2021**, *46*, 5369–5376. [CrossRef]
21. Tolkach, Y.; Kristiansen, G. The heterogeneity of prostate cancer: A practical approach. *Pathobiology* **2018**, *85*, 108–116. [CrossRef]
22. Midiri, F.; Vernuccio, F.; Purpura, P.; Alongi, P.; Bartolotta, T.V. Multiparametric MRI and radiomics in prostate cancer: A review of the current literature. *Diagnostics* **2021**, *11*, 1829. [CrossRef]
23. Huang, T.B.; Shi, R.J.; Shang, J.W.; Zhao, R.Z.; Wang, Y.M.; Xia, W.; Wang, S.Q.; Tan, R.Y.; Hua, L.X. Challenges in magnetic resonance imaging-based detection of clinically significant prostate cancer in young patients: Two alternative approaches. *Quant. Imaging Med. Surg.* **2024**, *14*, 9419. [CrossRef] [PubMed]
24. Wallström, J.; Thimansson, E.; Andersson, J.; Karlsson, M.; Zackrisson, S.; Bratt, O.; Jäderling, F. An online national quality assessment survey of prostate MRI reading: Interreader variability in prostate volume measurement and PI-RADS classification. *Eur. J. Radiol. Open* **2025**, *14*, 100625. [CrossRef]
25. Franz, T.; Sicker, T.; Lueke, J.; Dinh, B.; Ho, T.P.; Spinos, T.; Horn, L.C.; Schaudinn, A.; Liatsikos, E.; Stolzenburg, J.U. To biopsy or not biopsy, that is the question-PI-RADS 3 prostate lesions–validation of clinical and radiological parameters for biopsy decision-making. *BMC Urol.* **2025**, *25*, 274. [CrossRef] [PubMed]
26. Brancato, V.; Aiello, M.; Basso, L.; Monti, S.; Palumbo, L.; Di Costanzo, G.; Salvatore, M.; Ragozzino, A.; Cavaliere, C. Evaluation of a multiparametric MRI radiomic-based approach for stratification of equivocal PI-RADS 3 and upgraded PI-RADS 4 prostatic lesions. *Sci. Rep.* **2021**, *11*, 643. [CrossRef] [PubMed]
27. Tang, J.; Zheng, X.; Wang, X.; Mao, Q.; Xie, L.; Wang, R. Computer-aided detection of prostate cancer in early stages using multi-parameter MRI: A promising approach for early diagnosis. *Technol. Health Care* **2024**, *32*, 125–133. [CrossRef]

28. Zhang, G.M.; Han, Y.Q.; Wei, J.W.; Qi, Y.F.; Gu, D.S.; Lei, J.; Yan, W.G.; Xiao, Y.; Xue, H.D.; Feng, F.; et al. Radiomics based on MRI as a biomarker to guide therapy by predicting upgrading of prostate cancer from biopsy to radical prostatectomy. *J. Magn. Reson. Imaging* **2020**, *52*, 1239–1248. [CrossRef]
29. Winkel, D.J.; Breit, H.C.; Shi, B.; Boll, D.T.; Seifert, H.H.; Wetterauer, C. Predicting clinically significant prostate cancer from quantitative image features including compressed sensing radial MRI of prostate perfusion using machine learning: Comparison with PI-RADS v2 assessment scores. *Quant. Imaging Med. Surg.* **2020**, *10*, 808–817. [CrossRef]
30. Li, M.; Yang, L.; Yue, Y.; Xu, J.; Huang, C.; Song, B. Use of radiomics to improve diagnostic performance of PI-RADS v2.1 in prostate cancer. *Front. Oncol.* **2021**, *10*, 631831. [CrossRef]
31. Winkel, D.J.; Breit, H.C.; Block, T.K.; Boll, D.T.; Heye, T.J. High spatiotemporal resolution dynamic contrast-enhanced MRI improves the image-based discrimination of histopathology risk groups of peripheral zone prostate cancer: A supervised machine learning approach. *Eur. Radiol.* **2020**, *30*, 4828–4837. [CrossRef] [PubMed]
32. Afshari Mirak, S.; Mohammadian Bajgiran, A.; Sung, K.; Asvadi, N.H.; Markovic, D.; Felker, E.R.; Lu, D.; Sisk, A.; Reiter, R.E.; Raman, S.S. Dynamic contrast-enhanced (DCE) MR imaging: The role of qualitative and quantitative parameters for evaluating prostate tumors stratified by Gleason score and PI-RADS v2. *Abdom. Radiol.* **2020**, *45*, 2225–2234. [CrossRef] [PubMed]
33. Delongchamps, N.B.; Rouanne, M.; Flam, T.; Beuvon, F.; Liberatore, M.; Zerbib, M.; Cornud, F. Multiparametric magnetic resonance imaging for the detection and localization of prostate cancer: Combination of T2-weighted, dynamic contrast-enhanced and diffusion-weighted imaging. *BJU Int.* **2011**, *107*, 1411–1418. [CrossRef] [PubMed]
34. Thulasi, Seetha, S.; Garanzini, E.; Tenconi, C.; Marenghi, C.; Avuzzi, B.; Catanzaro, M.; Stagni, S.; Villa, S.; Chiorda, B.N.; Badenchini, F.; et al. Stability of multi-parametric prostate MRI radiomic features to variations in segmentation. *J. Pers. Med.* **2023**, *13*, 1172. [CrossRef]
35. Vaitulevičius, A.; Bernatavičienė, J.; Markevičiutė, J.; Naruševičiūtė, I.; Trakymas, M.; Treigys, P. Advancements in prostate zone segmentation: Integrating attention mechanisms into the nnU-Net framework. *Mach. Learn. Sci. Technol.* **2024**, *5*, 045003. [CrossRef]
36. Pineda, F.D.; Medved, M.; Wang, S.; Fan, X.; Schacht, D.V.; Sennett, C.; Oto, A.; Newstead, G.M.; Abe, H.; Karczmar, G.S. Ultrafast bilateral DCE-MRI of the breast with conventional Fourier sampling: Preliminary evaluation of semi-quantitative analysis. *Acad. Radiol.* **2016**, *23*, 1137–1144. [CrossRef]